

Intelligent Industrial Motor Monitoring

Nick Bui, Mohamed Homsi, Aashrith Beesabathuni, Vincent Duong, Carter Chen
{nicholasqbui, mohamedhomsi, aashrith.b24, vincent_duong, carter16891}@berkeley.edu



Fig. 1: Industrial AC Motor

Abstract—Induction motors form the backbone of modern industrial systems, accounting for an estimated 90% of electrically driven machinery, including manufacturing robots, CNC machines, conveyor systems, HVAC infrastructure, and mission-critical aerospace applications such as those used by NASA for rovers, satellites, pumps, and control actuators. Despite their widespread use, induction motor-based systems are susceptible to mechanical and electrical faults, including bearing wear, shaft misalignment, and gear damage, that often remain undetected until catastrophic failure occurs. These faults manifest as excess power consumption, elevated operating temperatures, and characteristic shifts in vibration and current signatures. This work presents an intelligent industrial motor monitoring system that continuously analyzes 3-phase motor current, vibration, and temperature to enable early fault detection and improved system reliability. By leveraging the intrinsic relationship between electromagnetic induction, mechanical load, and resulting thermal and vibrational behavior, the proposed system captures health indicators that reflect both motor efficiency and mechanical integrity. Deviations from nominal operating patterns, such as increased heat generation, abnormal vibration spectra, and irregular current draw, are used to identify potential faults before failure. The resulting platform demonstrates a scalable, sensor-driven approach to real-time motor health monitoring suitable for a wide range of industrial and aerospace applications.

ACKNOWLEDGEMENTS

We would like to thank Professor Dutta, Paul De La Sayette, and Matteo Guerrera for providing invaluable guidance and contributions to the project. Secondly, we would like to thank Dr. Rodney Martin and Isak Bolin of the NASA Ames Research Center for providing the initial paper, which is the backbone upon which this project is built on.

1. INTRODUCTION

This research project is conducted in collaboration with the NASA Ames Research Center and builds upon the work presented in *Generalized Fault Detection of Broken Rotor Bars in Induction Motors Based on the Order Domain Transformer and the Filtered Park’s Vector Approach* [1] by Isak Bolin, advised by Dr. Rodney Martin. In that work, Bolin introduced a preprocessing framework that combines the Order Domain Transformer (ODT) with the Filtered Park’s Vector Approach (FPVA) to normalize stator current data across induction motors with differing specifications, enabling generalized detection of broken rotor bar faults without requiring prior knowledge of motor parameters or labeled data from the target machine. Induction motor-based industrial systems are also susceptible to faults such as misalignment, bearing wear, and gear damage, which often remain undetected until failure occurs. Motivated by the gap between algorithmic fault detection and deployable monitoring infrastructure, this project develops a physical implementation of an intelligent motor health monitoring platform that continuously acquires and analyzes motor current, vibration, and temperature signals to enable early fault detection and improve overall system reliability.

2. IMPLEMENTATION

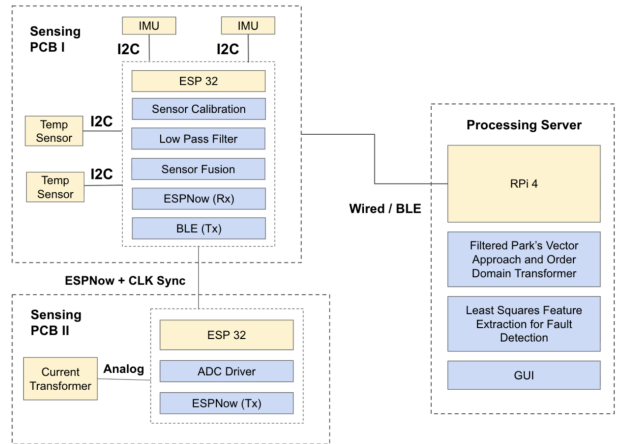


Fig. 2: System Architecture

At a high level, our implementation is comprised of 3 subsystems: a printed circuit board (PCB) that measures the motor’s temperature and vibration, a PCB that measures the motor’s 3-phase current draw, and a data processing

server where we deploy our fault detection algorithms and graphical user interface (GUI) [Fig. 2]. Data is transmitted from each PCB to the processing server either via a wired or wireless connection.

It is important to note that for this implementation, we did not have access to a traditional 3-phase induction motor. Instead, we used brushless motors with an electronic speed controller (ESC). 3-phase induction motors are powered with 3 individual sinusoidal waves 120 degrees apart [Fig. 3]. ESCs use pulse width modulation to produce 3 pulsating sawtooth waveforms to simulate a smooth 3-phase sinusoidal waveform [Fig. 4]. This difference would impact the results of our fault detection system compared to Isak's, but it still has applications to industrial motors.

2.1. Hardware

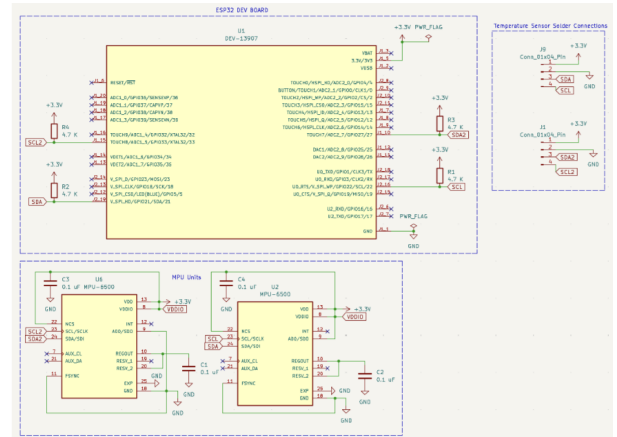


Fig. 5: Temperature & Vibration PCB Schematic

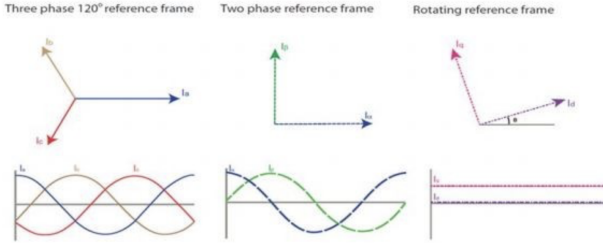


Fig. 3: 3-Phase Industrial Motor Waveform

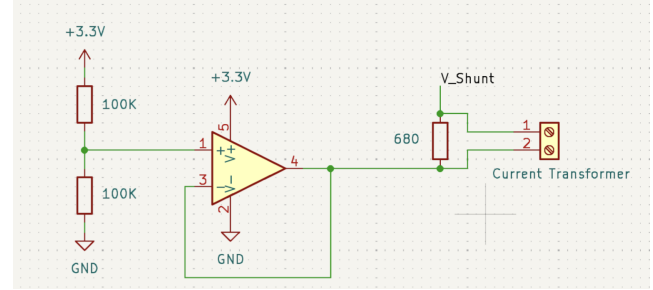


Fig. 6: Current Transformer Biasing Circuit

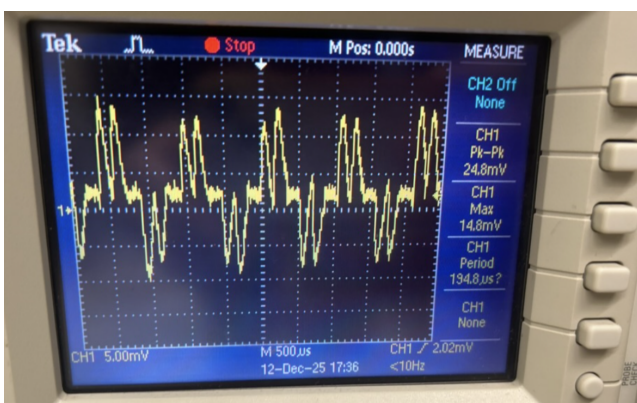


Fig. 4: Brushless ESC Waveform

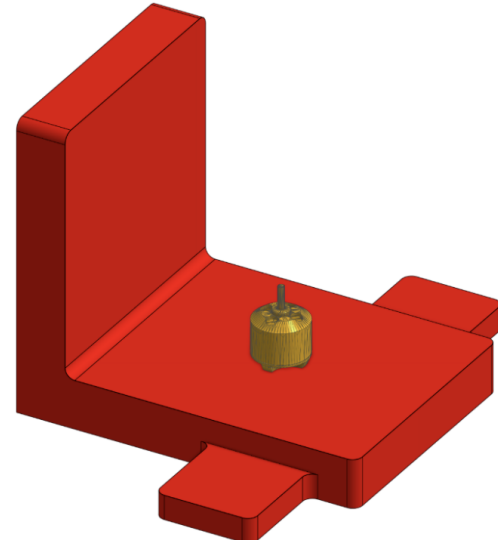


Fig. 7: Testing Rig CAD

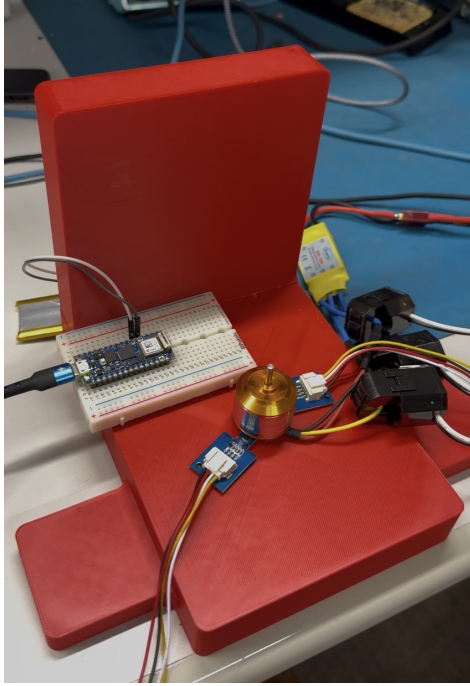


Fig. 8: Fully Assembled Testing Rig

2.11. Temperature and Vibration PCB: The temperature and vibration PCB [Fig. 5] measures the heat and vibration generated by the motor during operation. It consists of 2 SHT30 temperature sensors, which measure the motor’s temperature, and 2 MPU6500 inertial measurement units (IMUs), which measure the motor’s linear acceleration. These sensors are all connected to an ESP32 via the I2C bus. The temperature sensors are placed near the windings of our motor, and the IMUs are strapped onto the testing rig. We could not mount the sensors directly onto the motors, as we only had outrunner motors where the rotor spins around the stator.

2.12. Current Sensor PCB: The current sensor PCB measures the 3-phase current draw of our motors and is built upon a current transformer, a sensor that clips around the motor’s cables and measures its current draw by sensing the magnetic field produced by the AC current without having to make electrical contact. This current transformer is connected to an ADC input on the ESP32 that will read the AC waveform from the current transformer clamp [Fig. 6]. A shunt resistor is placed in parallel with the current transformer from which the ESP32 reads the induced voltage, which is used to compute the current [Eq. 1].

$$I = \frac{T_r (V_{shunt} - V_{bias})}{R_{shunt}} \quad (1)$$

By determining the value of the resistor, the amplitude of the voltage can be changed to fit the 3.3V range of the microcontroller. Since the ESP32’s ADC is rated from 0 - 3.3V, a voltage divider is required to bias the AC voltage. The bias is also put through a unity-gain buffer so that its

current is not loaded by the shunt resistor. An oscilloscope and high grade current clamp were used to verify the waveforms.

2.13. Physical Testing Rig: We designed and 3D printed a testing rig [Fig. 7] to mount our PCBs and motor in a secure manner, ensuring mechanical stability during operation, consistent sensor placement, and repeatable experimental conditions [Fig. 8].

2.2. Embedded Software

Using what we learned in EECS 149 about wired networking protocols, wireless communication, sensor calibration, signal conditioning, and signal sampling, we developed and integrated several custom embedded software packages throughout this project. If interested in reading the software we developed for this project, see our GitHub repository.

2.21. Sensor Drivers: Custom sensor drivers were implemented to interface with the IMU and temperature sensors over the I2C bus. These drivers handle device initialization, register configuration, and data acquisition through direct I2C transactions. Sensor-specific commands, register addresses, and configuration sequences were implemented by referencing the manufacturers’ datasheets to ensure correct operation and timing behavior. Raw sensor outputs were read from device registers and converted into digital values suitable for subsequent calibration and signal processing stages.

2.22. Affine Sensor Model: We used an affine sensor model to calibrate both the IMU and the temperature sensor by correcting for constant bias and sensor sensitivity. During calibration, each sensor was sampled multiple times under a known reference condition, and the average of the raw measurements was used to estimate the sensor bias. For the IMU, this reference was a stationary setup where the expected acceleration due to gravity was known, while for the temperature sensor, a known room temperature was used as ground truth. For all subsequent measurements, the estimated bias was subtracted from the raw sensor output, and the result was divided by the sensor sensitivity to obtain calibrated values in physical units [Eq. 2].

```

1: Initialize sum ← 0
2: for  $i = 1$  to  $N$  do
3:   Read raw sensor measurement  $y_{raw}$ 
4:   sum ← sum +  $y_{raw}$ 
5: end for
6: bias  $b \leftarrow \frac{\text{sum}}{\text{valid\_samples}} - y_{ref}$ 
```

$$y_{cal} = \frac{y_{raw} - b}{s} \quad (2)$$

2.23. Exponential Moving Average Low-Pass Filter: To reduce high-frequency noise in the calibrated temperature and acceleration signals, an exponential moving average (EMA) low-pass filter [Eq. 3] was applied to all sensor outputs. The EMA filter smooths incoming data by combining the current measurement with the previous filtered value using a weighting factor. This approach is computationally lightweight, requires minimal memory, and is well-suited for real-time embedded systems. The same filtering method was applied to both temperature and accelerometer data, with the smoothing factor chosen based on the desired trade-off between noise reduction and signal responsiveness.

$$y[n] = \alpha x[n] + (1 - \alpha) y[n - 1] \quad (3)$$

2.24. Bluetooth Low Energy: Bluetooth Low Energy (BLE) was used to transmit sensor data from an ESP32 to the processing server. After local calibration and filtering on the temperature and vibration PCB, temperature and vibration data were packaged into BLE packets and sent at a fixed update rate of 1kHz. BLE was chosen due to its low power consumption, built-in device discovery, and reliable short-range communication. This wireless link enabled real-time monitoring through the graphical user interface without requiring a wired connection during operation.

2.25. USB: Due to packet transmission latency associated with BLE and our data processing algorithms' dependency on phase-accurate current data sampled at high frequencies (1.5 kHz), we chose to package our 3-phase current data into a serial packet and send it from the current sensing PCB to the processing server via a wired USB connection at a transmission frequency of 10kHz. This allowed our current data to be sampled at a high frequency and transmitted with very low latency ($100\mu s$), ensuring the data processing algorithms deployed on our processing server received phase-accurate current data sampled at high frequencies.

2.3. Data Processing

Algorithm 1 Park's Vector Approach

Require: 3-phase stator currents $\{i_a[n], i_b[n], i_c[n]\}_{n=1}^N$

Ensure: d -axis and q -axis currents $\{i_d[n], i_q[n]\}_{n=1}^N$

```

1: for  $n = 1$  to  $N$  do
2:    $i_d[n] \leftarrow \sqrt{\frac{2}{3}} i_a[n] - \frac{1}{\sqrt{6}} i_b[n] - \frac{1}{\sqrt{6}} i_c[n]$ 
3:    $i_q[n] \leftarrow \frac{1}{\sqrt{2}} i_b[n] - \frac{1}{\sqrt{2}} i_c[n]$ 
4: end for
5: return  $\{i_d[n], i_q[n]\}_{n=1}^N$ 

```

3 current waveforms (i_a , i_b , i_c) are measured and then transformed using Park's Vector Approach to be analyzed into a two-dimensional space. The currents are now analyzed as the direct axis current (i_d) and quadrature axis current (i_q). The direct axis is aligned with the rotor's magnetic field and measures magnetic flux. The quadrature

axis is perpendicular to the direct axis and measures the torque produced.

2.4. Graphical User Interface

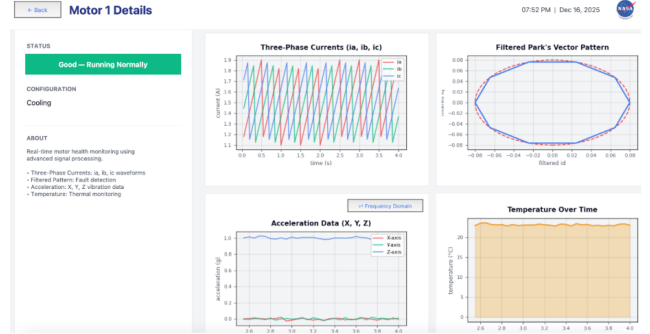


Fig. 9: Real-Time Motor Monitoring Dashboard GUI

The GUI is able to display 4 graphs, including the 3-phase current, the Filtered Park's Vector Approach based on the 3-phase current, accelerometer data, and temperature data. If thresholds are exceeded in any of the 4 measurements, the GUI will notify the user of the motor fault.

2.41. Triple Phase Current Monitoring: The graph in the top-left of the GUI displays the live 3-phase current waveforms as the motor operates. This allows the user to observe the instantaneous current in each phase and verify the relative phase offsets between them. By providing direct visibility into the electrical behavior of the motor, this graph helps confirm proper operation and serves as the input data source for further analysis.

2.42. Filtered Park's Vector Visualization: The graph in the top-right presents the filtered Park's Vector Transform of the 3-phase current data. This representation maps the phase currents into a two-dimensional space where motor faults are easier to detect. Under healthy operating conditions, the data forms a consistent and expected geometric pattern. Any deviation from this shape indicates abnormal behavior and potential faults that may not be obvious from the raw current waveforms alone.

2.43. Vibration and Frequency Analysis: The third graph shows accelerometer data collected from IMU sensors mounted on the motor rig. It displays real-time acceleration along the x, y, and z axes and computes the RMS vibration level. If the vibration exceeds a set threshold, the GUI flags a mechanical fault. In addition to the time-domain data, a Fast Fourier Transform (FFT) is performed to analyze vibration in the frequency domain. Industrial motors are expected to show a dominant frequency near 60 Hz, and the presence of additional dominant frequencies can indicate imbalance, misalignment, or other mechanical issues.

2.44. Temperature Monitoring: The final graph displays live temperature measurements taken near the motor windings. This graph enables continuous monitoring of the motor's thermal state during operation. If the temperature rises above a predefined safe threshold, the GUI issues a warning, indicating a potential overheating condition that could result from electrical faults, excessive load, or inadequate cooling.

3. TESTING

3.1. Forward Bias Waveform

A forward-bias diode was wired in series with a motor phase. This created a half-wave rectified waveform. In doing so, the motor would only twitch. Although only one waveform was physically rectified, it would rectify all 3 waveforms of the ESC. This is due to the ESC's control system, which analyzes one phase's waveform to calibrate the other two.

3.2. Off Centered Load

To simulate vibration, a 3D print was pressed fitted onto the motor. Since the brushless motor is an outrunner, its torque will also be applied to the 3D print. The print's center of mass is not aligned with the axis of rotation of the motor, creating a centrifugal force and vibration.

3.3. Temperature

Motors running at high throttle will inherently get hot. Two temperature sensors were placed below the windings of the motor. The average of the two will be measured.

4. CHALLENGES AND LIMITATIONS

4.1. Communication-Induced Phase Misalignment

A major challenge in our system was maintaining phase alignment in the measured 3-phase current signals. Before refactoring our codebase to use a USB connection for current data, the current data was transmitted from the current-sensing PCB to the temperature PCB using ESP-NOW and then forwarded to a computer over Bluetooth. This wireless communication pipeline introduced a random and non-deterministic delay in the received data, resulting in unpredictable phase shifts in the current waveforms. Because the Park's Vector Transform relies on accurate phase relationships between all 3 phases, these timing variations significantly distorted the transformed results and reduced consistency across trials.

4.2. Use of ESC-Driven Brushless Motors

Another limitation came from the type of motor used during testing. Due to the lack of access to an industrial 3-phase induction motor, brushless motors driven by electronic speed controllers (ESCs) were used instead. Industrial motors are typically powered by 3 sinusoidal waveforms phase-shifted by 120 degrees, whereas ESCs use a six-step commutation scheme that generates pulsed sawtooth waveforms. Since Isak's Park's vector-based

fault detection model assumes ideal sinusoidal inputs, this difference resulted in altered transformed patterns. Specifically, a healthy motor produced a six-pointed star pattern rather than the expected circular Lissajous curve.

It is important to note that not all industrial motors are driven by purely sinusoidal waveforms. Many industrial systems use variable frequency drives (VFDs) to enable speed control. In these systems, the 3-phase AC supply is first rectified to DC and then inverted back to 3-phase AC, a process that mirrors how an ESC converts DC voltage into AC. In other words, all industrial motors are driven by sinusoidal waveforms, but some are driven by pulsed, sawtooth-like waveforms similar to those produced by ESCs.

Two of the four datasets referenced by Isak's Park involve motors controlled by variable frequency drives. Under such conditions, a six-pointed star pattern would also be expected in the Lissajous representation. The exact current measurement location in Isak's work is unclear; however, if the current was measured before the rectifier rather than after the inverter, this would explain why a circular Lissajous curve was observed instead of the six-pointed star pattern seen in our experiments.

4.3. High Sampling Rate Requirements

We also found that the current signals needed to be sampled well above the Nyquist rate in order for the Park's Vector Transform to produce usable results. A sampling rate of 10 kHz was required to accurately capture the high-frequency components introduced by the ESC's switching behavior. Lower sampling rates led to aliasing and distorted phase relationships, which further degraded the Park's Vector output. This requirement increased computational and communication load, placing additional constraints on the embedded system.

5. RESULTS FROM PARK'S VECTOR APPROACH

The Park's Vector Approach is commonly used as a motor health monitoring technique by transforming 3-phase stator currents into the rotating i_d - i_q reference frame. Under ideal conditions, when a motor is supplied with 3 balanced sinusoidal phase currents separated by 120 degrees, the transformed current forms a circular trajectory in the i_q versus i_d plane. This circular shape indicates balanced magnetic flux and constant torque production, and is typically associated with normal motor operation. Any deviation from this circular pattern is generally interpreted as an indication of a fault.

This expected behavior assumes that the motor is powered by a true industrial 3-phase supply that produces smooth sinusoidal currents. Figures 10a and 10b show Park's Vector plots obtained from ideal 3-phase AC motors. In the healthy case, the transformed currents form a near-perfect circle, as shown in Fig. 10a. When a fault such as a broken rotor bar is introduced, the circular trajectory becomes distorted and asymmetric, as shown in Fig. 10b.

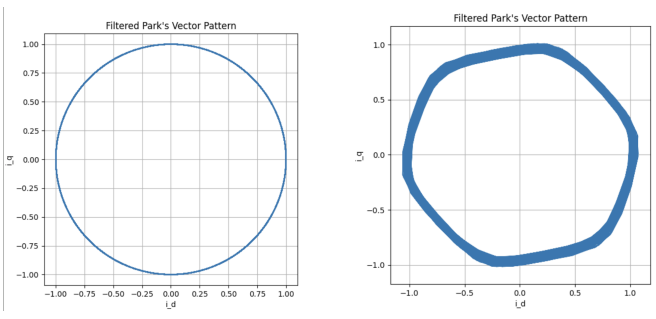


Fig. 10: Park's Vector pattern plots for ideal 3-phase industrial motors under healthy and faulty conditions.

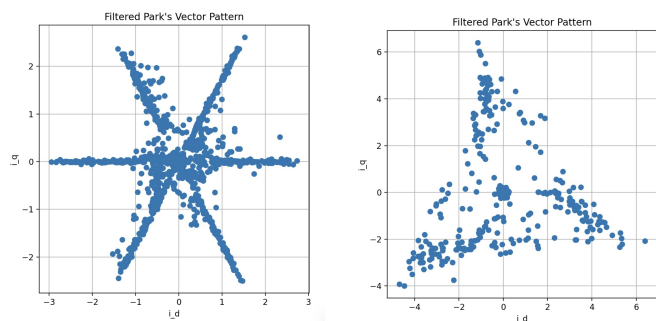


Fig. 11: Park's Vector plots for ESC-driven brushless motors under healthy and faulted conditions.

These results align with standard interpretations of the Park's Vector Approach for industrial induction motors.

In our experimental setup, however, the motors were driven by a six-step electronic speed controller (ESC) rather than an ideal 3-phase inverter. Brushless DC motors powered by ESCs do not generate continuous sinusoidal currents. Instead, the ESC switches between discrete commutation states based on rotor position, producing pulsed, sawtooth-like phase currents with significant harmonic content. Because the Park's Vector Transform assumes sinusoidal excitation, these non-ideal currents fundamentally change the resulting i_d - i_q trajectory.

When the Park's Vector Approach was applied to ESC-driven motors in our system, the expected circular pattern did not appear. Instead, for a healthy motor, the transformed currents consistently formed a six-pointed star shape, as shown in Fig. 11a. Each point of the star corresponds to one of the six commutation steps of the ESC, indicating that the discrete switching behavior directly influences the Park's Vector output. This pattern was repeatable across multiple trials and served as the baseline signature for normal operation under six-step commutation.

To evaluate fault sensitivity under ESC excitation, a

diode was placed in series with one phase to intentionally disrupt the current waveform and phase balance. This fault caused the Park's Vector trajectory to deviate significantly from the healthy six-pointed star. As shown in Fig. 11b, the transformed currents collapsed into a triangular and highly asymmetric pattern, accompanied by increased noise and dispersion. The exact shape depended on the severity of the disturbance, but in all cases the faulted patterns were clearly distinguishable from the healthy ESC baseline.

These results show that while the traditional interpretation of the Park's Vector Approach assumes sinusoidal excitation and circular trajectories, the method can be extended to motors driven by six-step ESCs by redefining the expected healthy signature. For ESC-driven brushless motors, a six-pointed star represents normal operation, while deviations from this shape indicate abnormal behavior. This suggests that the Park's Vector Approach is not limited to ideal industrial motors and can be applied to brushless motors commonly used in drones and small robotic systems, provided the motor drive method is taken into account.

6. CONCLUSION AND FUTURE WORK

We were able to successfully make a portable and simplified way to measure the health of a motor. We believe that this approach can be used for industrial motors and be expanded to brushless motor applications.

Future work to expand upon the results described in this paper will primarily include performing machine learning techniques on the collected data and build a multi-class classification model, with various features extracted from the acceleration, temperature, and current data collected. This would allow for a more granular level of detail that could be displayed to a hypothetical user, moving beyond mere detection of fault presence and into classifying what type of fault it could be. Additionally, securing the ability to test this implementation on industrial motors such as the ones at the Ames Research Center continues to be a top priority.

REFERENCES

- [1] I. Bolin, "Generalized fault detection of broken rotor bars in induction motors based on the order domain transformer and the filtered park's vector approach," master's thesis, Uppsala University, 2024.
- [2] D. Carletti, G. B. Ladislau, M. M. do Amaral, R. E. Volkers, W. J. Tozi, R. P. dos Santos, M. L. Ramos, T. O. dos Santos, and L. F. Encarnaçāo, "Synthetic dataset for induction motor broken rotor bar analysis," 2024.
- [3] A. Boushaba, S. Cauet, A. Chamroo, E. Etien, and L. Rambault, "Comparative study between physics-informed cnn and pca in induction motor broken bars mcsa detection," *Sensors*, vol. 22, no. 23, p. 9494, 2022.